Research Article Vol. 6, No. 11 / November 2019 / Optica 1416

Spontaneous photon-pair generation from a dielectric nanoantenna

Giuseppe Marino,[1,2,3,11] Alexander S. Solntsev,[1,4] Lei Xu,[1,5,9] Valerio F. Gili,[3] Luca Carletti,[6] Alexander N. Poddubny,[1,7,8] Mohsen Rahmani,[1] Daria A. Smirnova,[1] Haitao Chen,[1,5,9] Aristide Lemaître,[10] Guoquan Zhang,[9] Anatoly V. Zayats,[2] Costantino De Angelis,[6] Giuseppe Leo,[3] Andrey A. Sukhorukov,[1] and Dragomir N. Neshev[1,*]

[1]Nonlinear Physics Centre, Research School of Physics, Australian National University, Canberra ACT 2601, Australia
[2]Department of Physics and London Centre for Nanotechnology, King's College London, Strand, London WC2R 2LS, UK
[3]Matériaux et Phénomènes Quantiques, Université Paris Diderot-CNRS, F-75013 Paris, France
[4]School of Mathematical and Physical Sciences, University of Technology Sydney, 15 Broadway, Ultimo NSW 2007, Australia
[5]School of Engineering and Information Technology, University of New South Wales, Canberra ACT 2600, Australia
[6]Department of Information Engineering, University of Brescia, Via Branze 38, 25123 Brescia, Italy
[7]ITMO University, 49 Kronverksky Pr., Saint Petersburg 197101, Russia
[8]Ioffe Physical-Technical Institute, Saint Petersburg 194021, Russia
[9]The MOE Key Laboratory of Weak Light Nonlinear Photonics, School of Physics, Nankai University, Tianjin, China
[10]Centre de Nanosciences et de Nanotechnologies, CNRS, Universite Paris-Sud, Universite Paris-Saclay, C2N Marcoussis, F-91460, Marcoussis, France
[11]e-mail: Giuseppe.Marino@univ-paris-diderot.fr
*Corresponding author: Dragomir.Neshev@anu.edu.au

Received 5 July 2019; revised 27 September 2019; accepted 29 September 2019 (Doc. ID 371545); published 4 November 2019

Optical nanoantennas have shown a great capacity for efficient extraction of photons from the near to the far field, enabling directional emission from nanoscale single-photon sources. However, their potential for the generation and extraction of multi-photon quantum states remains unexplored. Here we experimentally demonstrate the nanoscale generation of two-photon quantum states at telecommunication wavelengths based on spontaneous parametric down-conversion in an optical nanoantenna. The antenna is a crystalline AlGaAs nanocylinder, possessing Mie-type resonances at both the pump and the bi-photon wavelengths, and when excited by a pump beam it generates photon pairs with a rate of 35 Hz. Normalized to the pump energy stored by the nanoantenna, this rate corresponds to 1.4 GHz/Wm, being 1 order of magnitude higher than conventional on-chip or bulk photon-pair sources. Our experiments open the way for multiplexing several antennas for coherent generation of multi-photon quantum states with complex spatial-mode entanglement and applications in free-space quantum communications and sensing.

https://doi.org/10.1364/OPTICA.6.001416

1. INTRODUCTION

Correlated photon pairs are essential building blocks for photon entanglement [1–3], which underpins many quantum applications including secure networks, enhanced measurement and lithography, and quantum information processing [4]. One of the most versatile techniques for the generation of correlated photons is the process of spontaneous parametric down-conversion (SPDC) [5]. The latter allows for an arbitrary choice of energy and momentum correlations between the generated photons, robust operation at room temperature, as well as spatial and temporal coherence between simultaneously pumped multiple SPDC sources.

Alternative approaches based on atom-like single-photon emitters such as solid-state fluorescent atomic defects [6], quantum dots [7,8], and 2D host materials [9,10], have reached a high degree of frequency indistinguishability, purity, and brightness [7,8]. However, this comes with the expense of operation at cryogenic temperatures and lack of spatial coherence between multiple quantum emitters. These features might limit possible applications and reduce the potential for device scalability. Furthermore, the small size of the atomic sources often requires complex schemes aimed at coupling to optical nanoantennas and improving the photon extraction efficiency [9].

The miniaturization of SPDC quantum-light sources to micro- and nanoscale dimensions is a continuing quest, as it enables denser integration of functional quantum devices. Traditionally, bulky centimeter-sized crystals were utilized for SPDC, entailing the difficulty of aligning multiple optical elements after the SPDC crystal while offering relatively low photon-pair rates [5]. As a first step of miniaturization, SPDC was realized in low-index-contrast waveguides, which allowed confining light down to several square micrometers transversely to the propagation direction, significantly

enhancing the conversion efficiency [11]. However, this approach still requires centimeters of propagation length, which makes the on-chip integration with other elements challenging [12]. The introduction of high-index-contrast waveguides and ring resonators allowed for shrinking the sizes necessary for SPDC to millimeters [13] and to tens of micrometers [14]. However, further miniaturization down to the nanoscale requires conceptually different approaches.

For a long time, plasmonic nanoantennas have been considered a favorable platform for enhancing single-photon emission [15,16] and nonlinear interactions [17–21]. However, the limited volume of the plasmonic modes, the losses, and the centrosymmetric nature of plasmonic materials result in a relatively low second-order nonlinear conversion efficiency. Dielectric nanoantennas have thus emerged as an alternative nanoscale nonlinear platform [22–26]. The strong enhancement of the nonlinear processes observed in them is largely due to the absence of material absorption and the excitation of Mie-type bulk resonances [27]. The highest conversion efficiency to date has been achieved employing III–V semiconductor nanostructures, such as AlGaAs, which is a non-centrosymmetric material with high quadratic nonlinear susceptibility. In particular, second-harmonic generation efficiencies up to 10^{-4} have been recently demonstrated [28–34], six orders of magnitude higher than in plasmonics.

Despite the rapid recent progress, the generation of quantum light with nonlinear nanoantennas has not been reported to date. Such nanoscale multi-photon quantum sources would offer an unexplored avenue for applications of highly indistinguishable and spatially reconfigurable quantum states through the spatial multiplexing of several coupled nanoantennas. Until now, the big question of whether a single nanoscale antenna can generate measurable pairs of photons with non-classical polarization and energy correlations remains open.

Here we experimentally demonstrate the generation of spontaneous photon pairs from a single AlGaAs disk nanoantenna exhibiting Mie-type resonances at both the pump and bi-photon wavelengths. In particular, a linearly polarized SPDC pump predominantly excites an electric dipole, which couples to orthogonal Cartesian components of the magnetic dipole at the signal and idler frequencies following the AlGaAs nonlinear tensor symmetry. As such, the generation of photon pairs is a result of the correlations between two subwavelength magnetic dipole modes. The observed photon-pair generation rate is 35 Hz, which, per unit volume, reaches values of up to 1.4 GHz/Wm, being orders of magnitude higher than both bulk and recent on-chip photon-pair sources [5,14,35]. Our SPDC source offers room-temperature operation and the possibility of both engineering the radiation pattern and obtaining coherent interference between multiplexed sources thanks to its inherent capacity to shape the subwavelength electromagnetic mode fields.

2. METHODS

We use a crystalline AlGaAs monolithic nanoantenna, since this material platform provides strong second-order nonlinear susceptibility. The fabrication steps follow the procedure developed in Ref. [28]. The AlGaAs layers are grown by molecular-beam epitaxy on [100] non-intentionally doped GaAs wafer. A 400 nm layer of $Al_{0.18}Ga_{0.82}As$ sits on top of a 1 μm thick $Al_{0.98}Ga_{0.02}As$ substrate sandwiched between two transition regions with varying aluminum molar fraction in order to improve the eventual optical quality of the interface between AlOx and the adjacent crystalline layers. Patterned circles with radii of 215 nm and equally spaced by 10 μm were produced with a scanning electron microscope (SEM) lithography system. It followed a dry etching of the sample with non-selective inductively coupled plasma–reactive ion etching (ICP-RIE) with $SiCl_4$:Ar chemical treatment. The etching depth of 400 nm, controlled by laser interferometer, defined the nanocylinders and revealed the AlAs layer. The etched sample was then oxidized at 390°C for 30 min in an oven equipped with *in situ* optical monitoring under a precisely controlled water vapor flow with N_2:H_2 gas carrier. After oxidation, each $Al_{0.18}Ga_{0.82}As$ nanocylinder lies upon a uniform AlOx substrate, whose low refractive index enables subwavelength optical confinement in the nanocavity by total internal reflection. An SEM image of the AlGaAs nanocylinders is presented in Fig. 1(b).

The experimental demonstration of spontaneous photon pair generation in AlGaAs nanocylinders is carried out by measuring the second-order correlation $g^{(2)} = R_c/(R_1R_2\tau_c)$ using a beam splitter and two single-photon detectors at both outputs of this beam splitter [14,36]. Here R_c is the rate of coincidences between the detectors, corresponding to SPDC, while $R_{acc} = R_1R_2\tau_c$ is the accidental coincidence rate that includes the count rates on each detector R_1 and R_2. The coincidence time window is τ_c. We expect maximum $g^{(2)}$ at the zero time delay for the simultaneous arrival of the two photons [37]. A single-frequency diode pump laser (Xtra II, Toptica) with a central wavelength of 785 nm and a linewidth of <10 MHz, horizontally polarized, pumps the

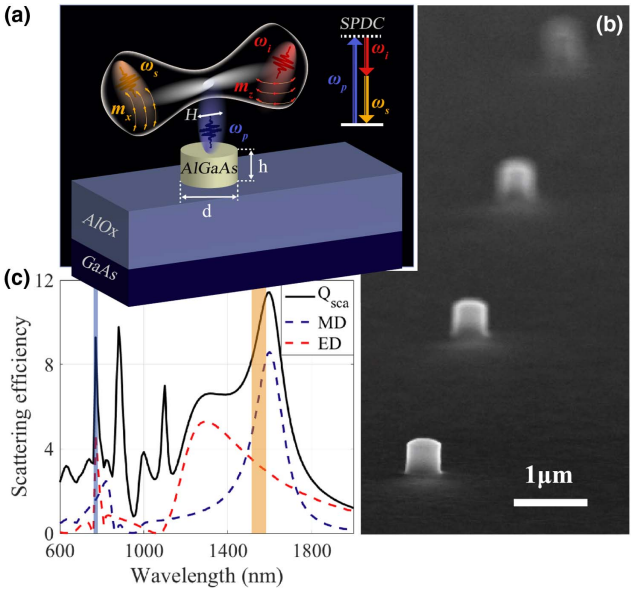

Fig. 1. Nonlinear nanoantenna for generation of spontaneous photon pairs. (a) Schematic representation of the nanoantenna-based source of photon pairs through the SPDC process. The inset depicts the energy diagram of the SPDC process. The SPDC pump is horizontally polarized along the [100] AlGaAs crystallographic axis. The signal and idler photons are generated by entangled magnetic dipole moments inside the volume of the AlGaAs nanoantenna, namely, m_x and m_z (sketched below the emitted photons). (b) Typical SEM images of [100] AlGaAs monolithic nanocylinders, 10 μm apart, such that each disk can be excited individually. (c) Simulated scattering efficiency Q_{sca} and multipolar decomposition in terms of the two leading electric (ED) and magnetic dipoles (MD) for a nanocylinder with diameter $d = 430$ nm and height $h = 400$ nm. The vertical blue and orange bars show the spectral ranges of the pump light and the generated SPDC light (signal and idler), respectively.

nanoantenna at normal incidence via a 0.7 NA objective (as shown in Fig. S4 of Supplement 1). The choice of the CW laser is justified by the fact that the SPDC photon-pair generation rate scales linearly with the average pump power. Furthermore, the CW operation allows us to eliminate the time-correlated noise if a pulsed pump was used, since a CW source has a flat temporal profile and a coherence time >100 ns, which is larger than the measured coincidence time range of 40 ns. The reflected SPDC signal and idler photon pairs can have different frequencies (ω_s and ω_i) and polarizations, can propagate at different angles with respect to the incident pump photons, and are collected in reflection geometry. They are then separated from the pump with a dichroic mirror and further filtered in free space from the residual pump with the use of three long-pass filters at 1100 nm. The photon pairs are then separated by a 50:50 beam splitter into two paths, and coincidences are measured with two gated InGaAs avalanche photodiodes (IDQ230) and a time-tagging module (ID801-TDC). The detectors are coupled with multi-mode fibers and operate at −90°C with an efficiency of 10% and dark counts of 5 Hz. The counting scheme consisted of a coincidence window of 300 bins with a bin width of $\tau_c = 162$ ps. The time difference between signal and idler was calibrated via replacing the (Xtra II, Toptica) single-frequency diode pump laser with a (Toptica Fiber Pro) femtosecond laser with a central wavelength 1560 nm. The linearly reflected beam was then collected by the same objective, divided into two beams propagating in the signal and idler collection arms by the 50:50 beam splitter, and detected from the two single-photon detectors, resulting in a coincidence time of 26.5 ns.

As the investigation of non-trivial polarization correlations directly through SPDC measurements is impractical due to the weak generation rate of AlGaAs nanocylinder sources, we first resort to the experimental investigation of sum-frequency generation (SFG). This is possible due to the recently established quantum-classical correspondence between the SPDC and SFG processes [38]. In the SFG experiment, the pulsed signal and idler beams are derived from a broadband femtosecond laser with a repetition rate of 80 MHz (Toptica, FibrePro). The two pulses are generated by spectrally slicing the 100 fs long pulses (bandwidth of 80 nm) into two paths at central wavelengths of 1520 and 1560 nm. After appropriate polarization conversion via the use of half- and quarter-wave plates, the two pulses are recombined with a 50:50 beam splitter and focused onto the nanoantenna at normal incidence by a 0.7 NA objective (as shown in Fig. S4 of Supplement 1). The reflected SFG radiation is collected in reflection through the same objective and separated from the signal and idler by a dichroic mirror. A short-pass filter at 800 nm is subsequently used for removal of the photoluminescence from the substrate, while a long-pass filter at 600 nm is used to remove the third-harmonic emission from the nanocylinder. The SFG emission is then acquired with a spectrometer or with a cooled camera in the real space. An additional confocal lens focusing at the objective's back focal plane is used for imaging the emission pattern in the Fourier space.

The linear and nonlinear responses of the AlGaAs nanoantenna are further modelled numerically using the finite element method solver in COMSOL Multiphysics in the frequency domain. The material dispersion of AlGaAs is taken from Ref. [39]. The second-order nonlinear susceptibility tensor of the [100] grown AlGaAs, possessing a zinc blend crystalline structure, is anisotropic and contains only off-diagonal elements $\chi^{(2)}_{ijk}$ with $i \neq j \neq k$. For the SFG process, assuming an undepleted pump approximation, we follow two steps. First, we simulate linear scattering at the fundamental wavelengths λ_s and λ_i. The bulk nonlinear polarization induced inside the particle is then employed as a source for the electromagnetic simulation to obtain the generated sum-frequency field. We further estimate the SPDC output correlation using quantum-classical correspondence [38]. The estimation is based on the calculated SF field and the field at the signal and idler wavelengths λ_s and λ_i as formulated below. The Q factors of the resonances reflect the enhancement of the SFG process and are estimated by calculating the complex frequency of resonances around the fundamental and harmonic wavelengths using the FEM solver through eigenfrequency analysis in COMSOL Multiphysics.

3. RESULTS AND DISCUSSION

A schematic of our nanoantenna photon-pair source is shown in Fig. 1(a). The nanoantenna is a crystalline AlGaAs cylinder with diameter $d = 430$ nm and height $h = 400$ nm. The SEM image of the fabricated structure is shown in Fig. 1(b). The noncentrosymmetric crystalline structure of AlGaAs offers strong bulk quadratic susceptibility of $d_{14} = 100$ pm/V [40,41]. The AlGaAs also exhibits high transparency in a broad spectral window from 730 nm up to the far infrared, due to the direct electronic bandgap, further preventing two-photon absorption at telecommunication wavelengths. As the distance between neighboring nanoresonators is 10 μm, the response is dominated by the local optical properties of the single constitutive nanoresonators. The dimensions of the nanocylinder are chosen such that it exhibits Mie-type resonances at the pump and signal/idler wavelengths. The simulated linear scattering efficiency is defined as the scattering cross section C_{sca} normalized by the cross area of the nanocylinder πr^2: $Q_{\text{sca}} = C_{\text{sca}}/\pi r^2$. It is shown in Fig. 1(c), along with the two leading multipolar contributions of the scattering. In the infrared region of the spectrum, where the signal and idler photon pairs are generated, the nanocylinder exhibits a magnetic dipolar resonance, which is the lowest-order Mie mode, featuring a Q factor of 9 [Fig. 1(c)]. For the spectral region of the pump, 760–790 nm, we have another strong resonance with a Q factor of 52, represented by a peak in the scattering efficiency spectrum [Fig. 1(c)]. This is dominated by the electric dipole moment of the antenna, although it also contains higher-order multipolar contributions (not shown). A more detailed study, including simulations of the scattering from nanoantennas with slightly different dimensions and measured reflectance around the SPDC pump, signal, and idler wavelengths, is reported in Section 2 of Supplement 1. The strong internal fields at the Mie-type resonances allow for strong enhancement of the nonlinear frequency mixing processes and also impose a spectral selection for the frequencies of the generated photons.

The SPDC process in the nanocylinder can result in the emission of photon pairs with nontrivial correlations, associated with different angular and polarization components. In order to experimentally determine the optimal conditions for photon-pair generation and ultimately for optimum SPDC efficiency, usually one uses the technique of quantum-state tomography [42].

However, due to weak generation rate of spontaneous processes, the bi-photon rate tends to be low, thereby resulting in long time acquisition of the photon counting statistics as well as lack of correlation precision. Therefore, optimizing the experimental

parameters directly through SPDC measurements is impractical, and we need an alternative solution.

To solve this issue, we resort to the quantum-classical correspondence between SPDC and its reversed process, namely, SFG, where the generated sum-frequency and pump waves propagate in opposite directions to the SPDC pump, signal, and idler [38,43]. Such quantum-classical correspondence is applicable to any quadratic nonlinear structure and allows the classical estimation of the SPDC generation bi-photon rates through the relation

$$\frac{1}{\Phi_p}\frac{dN_{\text{pair}}}{dt} = 2\pi\Xi^{\text{SFG}}\frac{\lambda_p^4}{\lambda_s^3\lambda_i^3}\frac{c\Delta\lambda}{\lambda_s^2}. \quad (1)$$

Here Φ_p is the SPDC pump flux; λ_p, λ_s, and λ_i are the pump, signal, and idler wavelengths; and $\Delta\lambda$ is the nonlinear resonance bandwidth at the signal/idler wavelengths. The efficiency Ξ^{SFG} is given by the ratio of sum-frequency photon power to the product of incident energy fluxes at the signal and idler frequencies. Detailed derivation of Eq. (1), along with its angular- and polarization-resolved versions, are given in Section 1.1 of Supplement 1. We establish that the number of photon pairs generated through SPDC, in a given optical mode of the nanostructure, is proportional to the SFG amplitude of the classical signal and idler waves, propagating in the opposite direction. In this framework, we can first optimize the SFG efficiency and thus predict the bi-photon generation rates prior to SPDC detection. Importantly, the SFG process can also be characterized for different polarizations, further optimizing the parameters for the subsequent SPDC measurements.

The schematic of our SFG experiments is illustrated in Fig. 2(a). The two short pulses at wavelengths 1520 and 1560 nm illuminate the nanoantenna as signal and idler beams. Their spectra are shown in Fig. 2(b). The two beams are focused onto a single AlGaAs nanocylinder by a 0.7 NA objective, with 10 mW average powers, 2 μm (diameter) diffraction-limited spots, and 7 GW/cm^2 peak intensities. The incident linear H polarization is parallel to the AlGaAs nanoresonator's crystallographic axis [100]. Figure 2(c) shows the H-polarized SFG signal collected in the backward direction at different optical delays between the two V-polarized pulses. This polarization arrangement corresponds to the maximum SFG efficiency as we discuss below. The two spectral peaks at 760 and 780 nm correspond to the second-harmonic generation (SHG) from the individual signal and idler pulses, and they are observed at all delay times. The third peak at 770 nm only occurs at "time zero," when the signal and idler pulses arrive at the nanocylinder simultaneously. This SFG pulse has a full width at half-maximum (FWHM) of 80 fs, in agreement with the duration of the pump pulses.

By setting different combinations of incident polarizations for the signal and idler pulses, including horizontal (H), vertical (V), right circular (R), and left circular (L), we measured the SFG for H (or V) polarization. The choice for H-polarized SFG is arbitrary, as for normally incident signal/idler beams V and H are identical due to the cylindrical symmetry of the disk and the isotropy of the material. The resulting SFG signal intensities (normalized to the maximum value) at 770 nm, and the corresponding radiation patterns recorded via a back focal plane (BFP) imaging system are shown in Figs. 2(d) and 2(e), respectively.

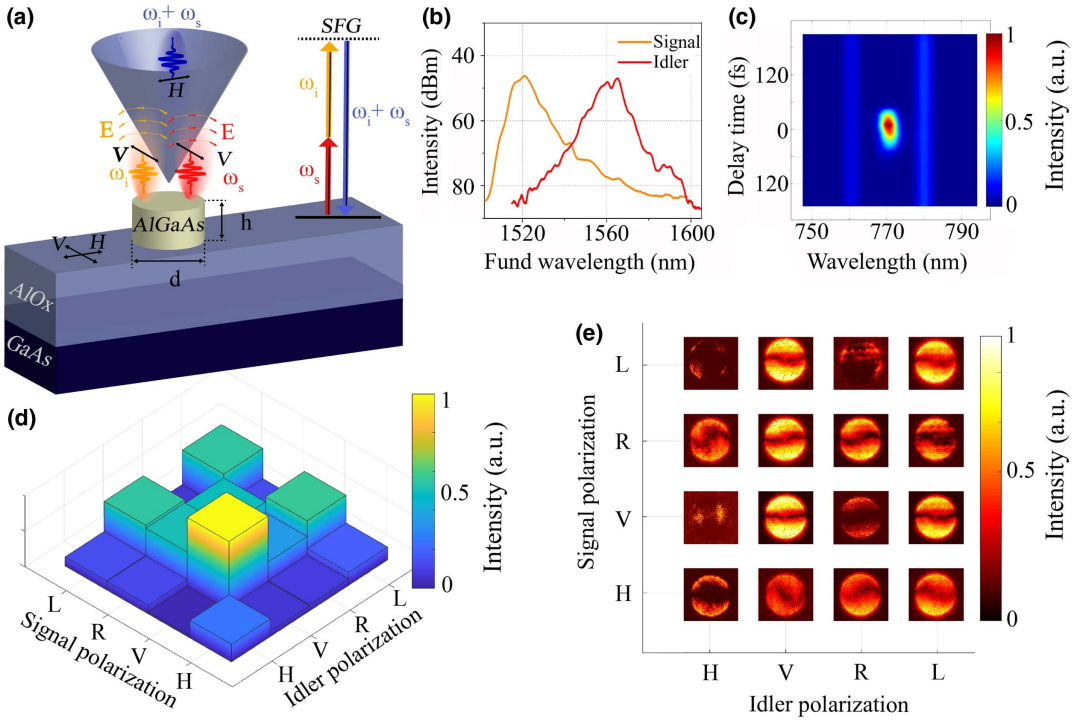

Fig. 2. SFG nonlinear characterization of polarization correlations in the nanoantenna. (a) Schematic of the experimental arrangement and energy conservation diagram of the SFG process in the inset. (b) Signal (orange line) and idler (red line) spectra filtered from the femtosecond laser source. (c) Spectrum of the nonlinear wave mixing in the AlGaAs nanocylinder as a function of the time delay between the signal and idler pulses. The SFG only happens when the two pulses overlap, while the spectral features at 760 and 780 nm correspond to SHG from the individual signal and idler pulses. (d) Intensity of H-polarized reflected SFG at 770 nm measured with 16 combinations of horizontal (H), vertical (V), right circular (R), and left circular (L) polarizations of the signal and idler beams for the nanocylinder geometry in Fig. 1. (e) Measured reflected SFG images in k-space for the polarization combinations shown in (d) and SFG detected with NA = 0.7.

The maximum signal of H-polarized SFG is obtained when both signal and idler are V polarized. At the microscopic scale, this corresponds to the excitation of signal, idler, and SFG modes whose vectorial components constructively overlap following the symmetry of AlGaAs second-order susceptibility tensor. The highest measured SFG conversion efficiency from our nanocylinder is 1.8×10^{-5} (see Supplement 1 Section 1.2), which is comparable to the SHG efficiency obtained in earlier measurements [28–30]. As shown in the BFP images, the SFG radiation patterns strongly depend on signal and idler polarization combinations; however, the general observation is that the SFG signal is emitted under the angle, off-axis to the nanocylinder. This is due to the symmetry of the nonlinear tensor as previously reported for SHG in Refs. [30,44]. The experimental results were also compared with finite-element simulations under realistic experimental conditions and are shown in Fig. S5 of Supplement 1. The simulated SFG intensity is enhanced when the polarizations of both the signal and idler beams are VV, or RR or LL polarized. Lower counts are seen for the mixed polarization cases and for the HH case. This trend matches the experimental results, particularly for the combinations involving H and V polarizations, while the RR and LL cases appears less bright than the VV case. This discrepancy can be attributed to slight nonuniformity of the fabricated structure, which has a small amount of ellipticity.

Importantly, knowing the SFG efficiency of 1.8×10^{-5} for the VV → H process, we can estimate the possible bi-photon rates for detection of photon-pair rates from our nanoantenna SPDC source. Using Eq. (1) we predict a photon-pair generation rate of about 380 Hz at a pump power of 2 mW. This value is significant and well above the dark count rates for our detector of 5 Hz (for details on the count rate estimation see Section 1.2 of Supplement 1). However, for Eq. (1) to optimally predict SPDC experiments, we need to look for solutions of the SFG emission mainly directed backwards so to overlap constructively with a practical SPDC pump, i.e., normally incident and linearly polarized. As backward SFG is maximized for the signal and idler incident around 45 deg (see Supplement 1, Fig. S7) and then an SPDC pump normally incident will result in a high photon-pair rate with oblique emission around 45 deg. In a SPDC experiment where collection is carried out by a NA = 0.7 objective, these photon pairs will be partially collected, so a smaller experimental count rate is expected compared to the theoretically predicted rate.

Detection of coincidences between photons generated through SPDC in the nanocylinder is illustrated in Fig. 1(a). The CW pump laser at 785 nm was incident with a power of 2 mW and a 2 μm (diameter) diffraction-limited spot. The generated photon pairs are expected to have a large spectral bandwidth of about 150 nm due to the broad magnetic dipole resonance in the IR spectral range as shown in Fig. 1(c). This bandwidth is quite broad with respect to conventional SPDC sources, which have typical sub-nanometer or few-nanometer bandwidth. This broad bandwidth offers a range of advantages, including a short temporal width for timing-critical measurements, such as for temporal entanglement [45] or for SPDC spectroscopy [46]. It also dictates a sub-100 fs temporal width of the generated photons, which is much shorter than the coincidence window τ_c. The measured coincidences for an H-polarized CW pump are presented in Fig. 3(a), where photon counting statistics are accumulated by integrating over 24 h. For a time difference of 26.5 ns, corresponding exactly to the time difference between the signal and idler previously calibrated (see the

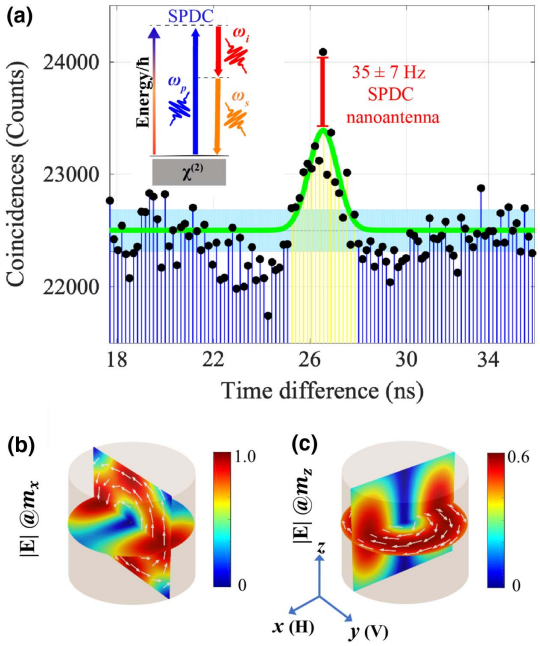

Fig. 3. Generation of photon pairs in an AlGaAs disk nanoantenna. IR coincidence counts integrated over 24 h on two single-photon detectors after a beam splitter (shown in Fig. S8 of Supplement 1). A significant statistical increase, marked by the red bar, is apparent at a time difference of 26.5 ns, corresponding to the temporal delay between both detectors. Black dots are the measured coincidences, the yellow shadowed area indicates correlation due to thermal excitation of the semiconductor materials, while the green line is its fitted Gaussian curve. The light blue shading represents the statistical error of the background. The inset shows a schematic of the SPDC process and energy correlation. (b) and (c) Numerically simulated fields inside the nanocylinder when exciting m_x and m_z modes, respectively. The white arrows indicate the electric field vector. Different color bar scales are used, following the different intensities of m_x, m_z inside the nanocylinder, in contrast to the symmetric case of a nanosphere.

Methods section), we observe a single bin with high coincidence rate. This is consistent with the physics of SPDC generation of signal and idler photons with the estimated temporal correlations of sub-100 fs. This peak of coincidence rate is statistically relevant and larger than the statistical error of 188 counts (shot-noise limit of 150 counts). We also observe the indication of correlation due to thermal excitation of the semiconductor materials [47] with approximately 2 ns width as shown with the yellow-shadowed area and its Gaussian fit (green line) in Fig. 3(a). We analyze the experimental SPDC rate from the AlGaAs nanocylinder, taking into account the losses in the detection system (see Section 6 of Supplement 1), and estimate the total photon-pair generation rate from our nanoantenna of $dN^{\text{gen}}_{\text{disk}}/dt = 35$ Hz. Normalized to the pump energy stored by the nanoantenna, this rate reaches values of up to 1.4 GHz/Wm, being 1 order of magnitude higher than conventional on-chip or bulk photon-pair sources [5,14] (for details, see Section 9 of Supplement 1).

Interestingly, this rate is significantly higher than the reference measurements of the AlOx/GaAs substrate without the nanocylinder (see Fig. S9 of Supplement 1), and it is estimated at $dN^{\text{gen}}_{\text{sub}}/dt = 9$ Hz. We also note that the SPDC from the substrate is generated in a diffraction-limited volume, which is more than 800 times larger than the volume of the nanoantenna.

The figure of merit calculated for this substrate source results in it being 4 orders of magnitude smaller than the nanocylinder (see Section 9 of Supplement 1). Besides the nanocylinder photon-pair rate being weak in absolute values, its high figure of merit reflects nanometer spatial confinements and relatively high Q factors achievable in AlGaAs nanostructures. The latter, operating in the Mie scattering regime, enables a fine shaping of the spectral and radiation profile, thereby leading to flexible quantum-state engineering and spatial multiplexing of SPDC sources via metasurfaces. We have also considered the likely influence of the AlGaAs nanocylinder on the SPDC from the substrate, such as refocusing the pump beam or the photon pairs; however, these were found to be negligible (see Section 8 of Supplement 1).

Finally, we have numerically calculated the photon correlation, shown in Fig. S12 of Supplement 1, to identify the origin of the measured correlation of Fig. 3(a). Only orthogonal Cartesian components of the magnetic dipole contribute to the SPDC process, which leads to coupling of two magnetic dipole moments of the nanoantenna, namely, m_x and m_z. The two coupled modes for an H-polarized pump beam are shown in Figs. 3(b) and 3(c). The coupling of these two subwavelength modes efficiently generates photon pairs in the far field via the antenna radiation and underpins the measured photon correlation.

We note that similar SPDC nanoscale sources can be obtained with other nonlinear crystalline nanostructures, making our approach of interest to the wider quantum community.

4. CONCLUSION

We have experimentally demonstrated the generation of bi-photon states in an AlGaAs nanoantenna via SPDC. We have first inferred the polarization correlation of the generated photon pairs via the quantum-classical correspondence with the reversed SFG process. SFG polarization maps and radiation diagrams not only allowed us to determine the efficiency of nonlinear interactions in the resonator but also reveal the directionality of the nonlinear emission. Second, we have experimentally demonstrated, for the first time to our knowledge, a spontaneous photon-pair source at the nanoscale with a bi-photon rate of up to 35 Hz. This is significantly higher than conventional SPDC photon sources when normalized to the pump energy stored by the nanoantenna. In the future, possible ways to increase both the rate of photon-pair generation and detection are by tuning the incident wavelength and angle, using a doughnut-like cylindrical vector pump beam, optimizing the nanoantenna geometry, embedding nanoantennas in a transparent substrate (5-fold enhancement in the SHG efficiency [30]), or finally employing Fano-resonant nanostructures [23,48,49]. The demonstrated nanoscale two-photon source lends itself to flexible quantum-state engineering by possible tailoring of the spectral and radiation profile of the nanoantenna. We can also envisage the possibility of tailoring the quantum interference of the emission from multiple nanoantennas or metasurfaces for generation of complex spatially entangled states [50,51], unrestricted by longitudinal phase matching [52]. Our nanoantenna concept is not just limited to SPDC photon-pair generation but is also applicable to other multi-photon quantum sources. It can thus open new opportunities for quantum applications such as free-space communications.

Funding. Australian Research Council (DP150103733, DP160100619, DE180100070, DP190101559, DE170100250, DE190100430; UK Engineering and Physical Sciences Research Council (EP/M013812/1); PANAMA; NOMOS (ANR-18-CE24-0026); EU MULTIPLY program; Royal Society; Erasmus Mundus NANOPHI (5659/002-001); Russian President (MD-5791.2018); ERC iCOMM project (789340); Wolfson Foundation; National Natural Science Foundation of China (11774182, 91750204); Russian Foundation for Basic Research (18-29-20037, 18-32-20065).

Acknowledgment. We thank Kai Wang, Matthew Parry, Carlo Gigli, Frank Setzpfandt, Juergen Sautter, and Yuri Kivshar for the useful discussions.

See Supplement 1 for supporting content.

REFERENCES

1. M. Muller, S. Bounouar, K. D. Jons, M. Glassl, and P. Michler, "On-demand generation of indistinguishable polarization-entangled photon pairs," Nat. Photonics **8**, 224–228 (2014).
2. M. A. M. Versteegh, M. E. Reimer, K. D. Jons, D. Dalacu, P. J. Poole, A. Gulinatti, A. Giudice, and V. Zwiller, "Observation of strongly entangled photon pairs from a nanowire quantum dot," Nat. Commun. **5**, 5296–5298 (2014).
3. C. Reimer, M. Kues, P. Roztocki, B. Wetzel, F. Grazioso, B. E. Little, S. T. Chu, T. Johnston, Y. Bromberg, L. Caspani, D. J. Moss, and R. Morandotti, "Generation of multiphoton entangled quantum states by means of integrated frequency combs," Science **351**, 1176–1180 (2016).
4. J. L. O'Brien, A. Furusawa, and J. Vučković, "Photonic quantum technologies," Nat. Photonics **3**, 687–695 (2009).
5. P. G. Kwiat, K. Mattle, H. Weinfurter, A. Zeilinger, A. V. Sergienko, and Y. H. Shih, "New high-intensity source of polarization-entangled photon pairs," Phys. Rev. Lett. **75**, 4337–4341 (1995).
6. A. Sipahigil, R. E. Evans, D. D. Sukachev, M. J. Burek, J. Borregaard, M. K. Bhaskar, C. T. Nguyen, J. L. Pacheco, H. A. Atikian, C. Meuwly, R. M. Camacho, F. Jelezko, E. Bielejec, H. Park, M. Loncar, and M. D. Lukin, "An integrated diamond nanophotonics platform for quantum-optical networks," Science **354**, 847–850 (2016).
7. P. Senellart, G. Solomon, and A. White, "High-performance semiconductor quantum-dot single-photon sources," Nat. Nanotechnol. **12**, 1026–1039 (2017).
8. N. Somaschi, V. Giesz, L. De Santis, J. C. Loredo, M. P. Almeida, G. Hornecker, S. L. Portalupi, T. Grange, C. Anton, J. Demory, C. Gomez, I. Sagnes, N. D. Lanzillotti-Kimura, A. Lemaitre, A. Auffeves, A. G. White, L. Lanco, and P. Senellart, "Near-optimal single-photon sources in the solid state," Nat. Photonics **10**, 340–345 (2016).
9. I. Aharonovich, D. Englund, and M. Toth, "Solid-state single-photon emitters," Nat. Photonics **10**, 631–641 (2016).
10. T. T. Tran, K. Bray, M. J. Ford, M. Toth, and I. Aharonovich, "Quantum emission from hexagonal boron nitride monolayers," Nat. Nanotechnol. **11**, 37–42 (2016).
11. M. Fiorentino, S. M. Spillane, R. G. Beausoleil, T. D. Roberts, P. Battle, and M. W. Munro, "Spontaneous parametric down-conversion in periodically poled KTP waveguides and bulk crystals," Opt. Express **15**, 7479–7488 (2007).
12. A. S. Solntsev and A. A. Sukhorukov, "Path-entangled photon sources on nonlinear chips," Rev. Phys. **2**, 19–31 (2017).
13. A. Orieux, A. Eckstein, A. Lemaitre, P. Filloux, I. Favero, G. Leo, T. Coudreau, A. Keller, P. Milman, and S. Ducci, "Direct Bell states generation on a III-V semiconductor chip at room temperature," Phys. Rev. Lett. **110**, 160502 (2013).
14. X. Guo, C. L. Zou, C. Schuck, H. Jung, R. S. Cheng, and H. X. Tang, "Parametric down-conversion photon-pair source on a nanophotonic chip," Light Sci. Appl. **6**, e16249 (2017).
15. J. A. Schuller, E. S. Barnard, W. S. Cai, Y. C. Jun, J. S. White, and M. L. Brongersma, "Plasmonics for extreme light concentration and manipulation," Nat. Mater. **9**, 193–204 (2010).
16. A. G. Curto, G. Volpe, T. H. Taminiau, M. P. Kreuzer, R. Quidant, and N. F. van Hulst, "Unidirectional emission of a quantum dot coupled to a nanoantenna," Science **329**, 930–933 (2010).
17. M. Kauranen and A. V. Zayats, "Nonlinear plasmonics," Nat. Photonics **6**, 737–748 (2012).

18. M. Celebrano, X. F. Wu, M. Baselli, S. Grossmann, P. Biagioni, A. Locatelli, C. De Angelis, G. Cerullo, R. Osellame, B. Hecht, L. Duo, F. Ciccacci, and M. Finazzi, "Mode matching in multiresonant plasmonic nanoantennas for enhanced second harmonic generation," Nat. Nanotechnol. **10**, 412–417 (2015).
19. M. Baselli, A. L. Baudrion, L. Ghirardini, G. Pellegrini, E. Sakat, L. Carletti, A. Locatelli, C. De Angelis, P. Biagioni, L. Duo, M. Finazzi, P. M. Adam, and M. Celebrano, "Plasmon-enhanced second harmonic generation: from individual antennas to extended arrays," Plasmonics **12**, 1595–1600 (2017).
20. G. Marino, P. Segovia, A. V. Krasavin, P. Ginzburg, N. Olivier, G. A. Wurtz, and A. V. Zayats, "Second-harmonic generation from hyperbolic plasmonic nanorod metamaterial slab," Laser Photon. Rev. **12**, 1700189 (2018).
21. J. Lee, M. Tymchenko, C. Argyropoulos, P. Y. Chen, F. Lu, F. Demmerle, G. Boehm, M. C. Amann, A. Alu, and M. A. Belkin, "Giant nonlinear response from plasmonic metasurfaces coupled to intersubband transitions," Nature **511**, 65–69 (2014).
22. M. R. Shcherbakov, D. N. Neshev, B. Hopkins, A. S. Shorokhov, I. Staude, E. V. Melik-Gaykazyan, M. Decker, A. A. Ezhov, A. E. Miroshnichenko, I. Brener, A. A. Fedyanin, and Y. S. Kivshar, "Enhanced third-harmonic generation in silicon nanoparticles driven by magnetic response," Nano Lett. **14**, 6488–6492 (2014).
23. Y. M. Yang, W. Y. Wang, A. Boulesbaa, I. I. Kravchenko, D. P. Briggs, A. Puretzky, D. Geohegan, and J. Valentine, "Nonlinear Fano-resonant dielectric metasurfaces," Nano Lett. **15**, 7388–7393 (2015).
24. G. Grinblat, Y. Li, M. P. Nielsen, R. F. Oulton, and S. A. Maier, "Efficient third harmonic generation and nonlinear subwavelength imaging at a higher-order anapole mode in a single germanium nanodisk," ACS Nano **11**, 953–960 (2017).
25. L. Carletti, A. Locatelli, O. Stepanenko, G. Leo, and C. De Angelis, "Enhanced second-harmonic generation from magnetic resonance in AlGaAs nanoantennas," Opt. Express **23**, 26544–26550 (2015).
26. H. Liu, C. Guo, G. Vampa, J. L. Zhang, T. Sarmiento, M. Xiao, P. H. Bucksbaum, J. Vučković, S. Fan, and D. A. Reis, "Enhanced high-harmonic generation from an all-dielectric metasurface," Nat. Phys. **14**, 1006 (2018).
27. A. I. Kuznetsov, A. E. Miroshnichenko, M. L. Brongersma, Y. S. Kivshar, and B. Luk'yanchuk, "Optically resonant dielectric nanostructures," Science **354**, aag2472 (2016).
28. V. F. Gili, L. Carletti, A. Locatelli, D. Rocco, M. Finazzi, L. Ghirardini, I. Favero, C. Gomez, A. Lemaitre, M. Celebrano, C. De Angelis, and G. Leo, "Monolithic AlGaAs second-harmonic nanoantennas," Opt. Express **24**, 15965–15971 (2016).
29. S. Liu, M. B. Sinclair, S. Saravi, G. A. Keeler, Y. M. Yang, J. Reno, G. M. Peake, F. Setzpfandt, I. Staude, T. Pertsch, and I. Brener, "Resonantly enhanced second-harmonic generation using III-V semiconductor all-dielectric metasurfaces," Nano Lett. **16**, 5426–5432 (2016).
30. R. Camacho-Morales, M. Rahmani, S. Kruk, L. Wang, L. Xu, D. A. Smirnova, A. S. Solntsev, A. Miroshnichenko, H. H. Tan, F. Karouta, S. Naureen, K. Vora, L. Carletti, C. De Angelis, C. Jagadish, Y. S. Kivshar, and D. N. Neshev, "Nonlinear generation of vector beams from AlGaAs nanoantennas," Nano Lett. **16**, 7191–7197 (2016).
31. L. Carletti, D. Rocco, A. Locatelli, C. De Angelis, V. F. Gili, M. Ravaro, I. Favero, G. Leo, M. Finazzi, L. Ghirardini, M. Celebrano, G. Marino, and A. V. Zayats, "Controlling second-harmonic generation at the nanoscale with monolithic AlGaAs-on-AlOx antennas," Nanotechnology **28**, 114005 (2017).
32. S. Liu, P. P. Vabishchevich, A. Vaskin, J. L. Reno, G. A. Keeler, M. B. Sinclair, I. Staude, and I. Brener, "An all-dielectric metasurface as a broadband optical frequency mixer," Nat. Commun. **9**, 2506–2507 (2018).
33. F. J. Löchner, A. N. Fedotova, S. Liu, G. A. Keeler, G. M. Peake, S. Saravi, M. R. Shcherbakov, S. Burger, A. A. Fedyanin, I. Brener, T. Pertsch, F. Setzpfandt, and I. Staude, "Polarization-dependent second harmonic diffraction from resonant GaAs metasurfaces," ACS Photon. **5**, 1786–1793 (2018).
34. G. Marino, C. Gigli, D. Rocco, A. Lemaítre, I. Favero, C. De Angelis, and G. Leo, "Zero-order second harmonic generation from AlGaAs-on-insulator metasurfaces," ACS Photon. **6**, 1226–1231 (2019).
35. M. Förtsch, J. U. Fürst, C. Wittmann, D. Strekalov, A. Aiello, M. V. Chekhova, C. Silberhorn, G. Leuchs, and C. Marquardt, "A versatile source of single photons for quantum information processing," Nat. Commun. **4**, 1818 (2013).
36. E. Engin, D. Bonneau, C. M. Natarajan, A. S. Clark, M. G. Tanner, R. H. Hadfield, S. N. Dorenbos, V. Zwiller, K. Ohira, N. Suzuki, H. Yoshida, N. Iizuka, M. Ezaki, J. L. O'Brien, and M. G. Thompson, "Photon pair generation in a silicon micro-ring resonator with reverse bias enhancement," Opt. Express **21**, 27826–27834 (2013).
37. D. Klyshko, *Physical Foundations of Quantum Electronics* (World Scientific, 2011).
38. A. N. Poddubny, I. V. Iorsh, and A. A. Sukhorukov, "Generation of photon-plasmon quantum states in nonlinear hyperbolic metamaterials," Phys. Rev. Lett. **117**, 123901 (2016).
39. S. Gehrsitz, F. K. Reinhart, C. Gourgon, N. Herres, A. Vonlanthen, and H. Sigg, "The refractive index of $Al_xGa_{1-x}As$ below the band gap: accurate determination and empirical modeling," J. Appl. Phys. **87**, 7825–7837 (2000).
40. I. Shoji, T. Kondo, A. Kitamoto, M. Shirane, and R. Ito, "Absolute scale of second-order nonlinear-optical coefficients," J. Opt. Soc. Am. B **14**, 2268–2294 (1997).
41. M. Ohashi, T. Kondo, R. Ito, S. Fukatsu, Y. Shiraki, K. Kumata, and S. Kano, "Determination of quadratic nonlinear optical coefficient of Al_x GA_{1-x} as system by the method of reflected second harmonics," J. Appl. Phys. **74**, 596–601 (1993).
42. D. F. V. James, P. G. Kwiat, W. J. Munro, and A. G. White, "Measurement of qubits," Phys. Rev. A **64**, 052312 (2001).
43. F. Lenzini, A. N. Poddubny, J. Titchener, P. Fisher, A. Boes, S. Kasture, B. Haylock, M. Villa, A. Mitchell, A. S. Solntsev, A. A. Sukhorukov, and M. Lobino, "Direct characterization of a nonlinear photonic circuit's wave function with laser light," Light Sci. Appl. **7**, 17143 (2018).
44. L. Carletti, A. Locatelli, D. Neshev, and C. De Angelis, "Shaping the radiation pattern of second-harmonic generation from AlGaAs dielectric nanoantennas," ACS Photon. **3**, 1500–1507 (2016).
45. S. Rogers, D. Mulkey, X. Y. Lu, W. C. Jiang, and Q. Lin, "High visibility time-energy entangled photons from a silicon nanophotonic chip," ACS Photon. **3**, 1754–1761 (2016).
46. A. S. Solntsev, P. Kumar, T. Pertsch, A. A. Sukhorukov, and F. Setzpfandt, "$LiNbO_3$ waveguides for integrated SPDC spectroscopy," APL Photon. **3**, 021301 (2018).
47. E. B. Flagg, S. V. Polyakov, T. Thomay, and G. S. Solomon, "Dynamics of nonclassical light from a single solid-state quantum emitter," Phys. Rev. Lett. **109**, 163601 (2012).
48. A. S. Shorokhov, E. V. Melik-Gaykazyan, D. A. Smirnova, B. Hopkins, K. E. Chong, D. Y. Choi, M. R. Shcherbakov, A. E. Miroshnichenko, D. N. Neshev, A. A. Fedyanin, and Y. S. Kivshar, "Multifold enhancement of third-harmonic generation in dielectric nanoparticles driven by magnetic Fano resonances," Nano Lett. **16**, 4857–4861 (2016).
49. P. P. Vabishchevich, S. Liu, M. B. Sinclair, G. A. Keeler, G. M. Peake, and I. Brener, "Enhanced second-harmonic generation using broken symmetry III–V semiconductor Fano metasurfaces," ACS Photon. **5**, 1685–1690 (2018).
50. K. Wang, J. G. Titchener, S. S. Kruk, L. Xu, H.-P. Chung, M. Parry, I. I. Kravchenko, Y.-H. Chen, A. S. Solntsev, Y. S. Kivshar, D. N. Neshev, and A. A. Sukhorukov, "Quantum metasurface for multiphoton interference and state reconstruction," Science **361**, 1104–1108 (2018).
51. T. Stav, A. Faerman, E. Maguid, D. Oren, V. Kleiner, E. Hasman, and M. Segev, "Quantum entanglement of the spin and orbital angular momentum of photons using metamaterials," Science **361**, 1101–1104 (2018).
52. C. Okoth, A. Cavanna, T. Santiago-Cruz, and M. V. Chekhova, "Microscale generation of entangled photons without momentum conservation," arXiv:1902.11218 (2019).